ACADEMIC
PRESS

Available online at www.sciencedirect.com
SCIENCE DIRECT®

Journal of Catalysis 215 (2003) 94–107

JOURNAL OF
CATALYSIS

www.elsevier.com/locate/jcat

Reactivity of Pt/ceria and Pt/alumina planar model catalysts prepared by colloidal lithography

L. Österlund,* S. Kielbassa, C. Werdinius, and B. Kasemo

Department of Applied Physics and Competence Centre for Catalysis, Chalmers University of Technology, SE-412 96 Göteborg, Sweden

Received 30 August 2002; revised 28 October 2002; accepted 28 October 2002

Abstract

We report on the structure, chemical state, and catalytic activity of nanofabricated, planar Pt/ceria and Pt/alumina model catalysts prepared by colloidal lithography. Employing extended etching times, catalyst particles are fabricated that are much smaller than the size of the polystyrene colloidal particle mask. Using CO oxidation as a probe reaction, the influence of various pretreatments has been studied. We find that the H_2/O_2 pretreatment deteriorates the reactivity on Pt/alumina, which is accompanied by blocking of the high-temperature CO adsorption sites as seen by TPD. After prolonged reactions the Pt/ceria particles show pronounced restructuring, indicating a low-temperature, reaction-induced, strong metal–support interaction, where ceria is decorating the Pt particles. In contrast, after an identical reaction history the Pt/alumina particles become facetted. The nanofabrication approach allows us to attribute the structural changes on individual particles to the integrated, macroscopic catalytic response.

Keywords: Nanofabrication; Colloidal lithography; Model catalyst; Pt/alumina; Pt/ceria; Strong metal-support interaction; CO oxidation; Pretreatments

1. Introduction

A long-term goal in fundamental catalysis research has been to synthesize and characterize supported catalyst particles with well-defined properties, e.g., well-defined size, shape, interparticle separation, and chemical environment (composition), in order to determine and correlate macroscopic reactivity with microscopic processes. So far, most fundamental studies have employed vapor deposition methods [1–4] and cluster source methods [5], which both allow controlled preparation and characterization under vacuum conditions. Driven by the rapid development of nanoscience and nanotechnology, new tools are today emerging, which find their way into a wide variety of research areas, such as novel biosensors [6], protein adsorption [7,8], and catalysis [9,10], which is our primary interest here.

In the present work we employ colloidal lithography to prepare well-defined planar nanocatalysts. The colloidal lithography method utilizes surface (self-) organization of colloidal particles (coming from a colloidal solution) to define a 2D nanopattern and surface etching techniques to develop the pattern. This makes possible the preparation of chemically well-defined model catalysts, while simultaneously ensuring a fast and versatile process. In a previous study we presented the fabrication method in detail [11]. Here we present a study of the catalytic activity of Pt/alumina and Pt/ceria model catalysts using CO oxidation as a probe reaction. We use a new method to reduce the metal particle size (here from 107 to 40 nm) without changing the colloidal template size. The particle size in this work was deliberately chosen to be large (40 nm) to facilitate iterative SEM analyses of the nanostructures before and after the reactions, despite the fact that the preparation method described here allows smaller particle sizes as well.

A large number of studies focus on the low-temperature oxidation of CO on alumina- and cerium oxide (ceria)-supported noble metal catalysts [12–19], which are important in a variety of applications, including automotive exhaust cleaning. Ceria is well known to readily change oxidation state ($Ce^{4+} \leftrightarrow Ce^{3+}$), which provides an oxygen storage function [20]. Very little quantitative information is, however, available for this latter function [21]. Apart from purely kinetic effects, resulting from spillover between the metal and the ceria support [14,21], electronic [22] and structural [18] modifications have been reported for ceria-

---

* Corresponding author.
E-mail address: lars.osterlund@fy.chalmers.se (L. Österlund).

0021-9517/03/$ – see front matter © 2003 Elsevier Science (USA). All rights reserved.
doi:10.1016/S0021-9517(02)00086-6

supported noble metals. The so-called strong metal-support interaction (SMSI) between an (easily) reducible support (such as ceria) and supported metal particles has been extensively studied [23]. It is associated with the formation of mixed metal–oxide species at the interface or metal particle decoration, which significantly modifies the chemical and catalytic properties of a catalyst. The behavior of the catalyst can, however, be restored by a high-temperature oxidation treatment. Typically SMSI is observed after high-temperature reduction treatments ($T \gtrsim 750$ K).

2. Experimental

2.1. Sample preparation

Silicon wafers with a thermally grown SiO_2 layer of thickness 3000 Å were used as primary substrates for colloidal lithography. Support films of either alumina or ceria were deposited onto the substrate by e-beam evaporation of pressed tablets made from a high-purity powder (99.9%) of aluminum oxide and cerium(IV) oxide in a sputter/evaporation chamber. This is known to result in the formation of an amorphous oxide phase [1–3]. Platinum was evaporated onto the support film by e-beam evaporation of a Pt sputter target (99.95% purity). Removal of the polystyrene (PS) mask was made by anisotropic etching of a rotating sample by directed Ar^+ bombardment at normal incidence at a beam energy of 500 V. A low-temperature oxygen plasma treatment was used to clean the Si substrate before the evaporation steps, before adsorption of the polystyrene particles, and also to remove polystyrene residues. Details of the sample preparation procedure can be found elsewhere [11].

2.2. Sample characterization

The CO oxidation measurements were performed in a microflow reactor operated with a very small gas flow (ca. 1 µl/s) designed for measurements on samples with very small catalyst loadings. In this study the samples were cut into 2 × 3 mm pieces. The details of the microflow reactor have been presented elsewhere [14,24]. The mass spectrometer signals were converted to a total conversion yield (%), using the calibrated CO_2 cracking pattern to obtain the correct CO content at $m/Z = 28$. In all CO oxidation reactor experiments the sample was heated with a linear heating ramp of 10 K/min. In some experiments, the sample was also cooled with the same T-ramp speed, and thus the hysteresis in the CO oxidation when going up and down in temperature could be measured [11]. All CO oxidation experiments were done in a oxygen excess at $\beta \equiv P_{CO}/(P_{CO} + P_{O_2}) = 0.1$ using 0.5% CO unless otherwise stated. Arrhenius plots were extracted in the kinetically controlled regime according to the procedure described in Ref. [11]. In all measurements, high-purity gas (research grade, Air Liquid) was used. The CO gas was in addition passed through a bed of activated carbon powder held at 150 °C to avoid carbonyl contamination, which previously was shown to influence CO oxidation on Pt/ceria catalysts prepared by electron beam lithography [14].

Temperature-programmed desorption (TPD) was performed in a UHV chamber pumped by a turbomolecular pump, giving a base pressure of 2×10^{-10} mbar. Pretreatments up to atmospheric pressure were done in a dedicated high-pressure cell, which was connected to the UHV chamber and separated from the main chamber by a gate valve. A base pressure of typically $\sim 10^{-9}$ mbar could be reached within 15 min after sample transfer from the high-pressure cell. The samples (1 × 1 cm) were clamped to an FeAl foil by a spring-loaded Macor piece and resistively heated from the back by passing a current through the FeAl foil. A thermocouple was pressed against the sample top surface by a spring-loaded Macor piece.

Structural characterisation of the samples was done by scanning electron microscopy (SEM, JEOL JSM-6301F). Tilted sample geometries ($> 85°$) and high beam voltage (30 kV) produced the best image quality, which provided simultaneous shape and size distributions of the nanoparticles. Image analysis was done by the software package Scion Image (Scion Image Corp.). To quantify the shape and size of the particles an average of the geometrical parameters was obtained from several high-resolution images (450,000× magnification) or > 50 particles.

Chemical analysis was done by X-ray photoelectron spectroscopy (XPS, Perkin–Elmer PHI 5000C ESCA system) employing 400-W Mg-K_α radiation, with the detector placed at 45° with respect to the surface. The binding energy calibration was done by internal calibration against the C 1s peak. Curve deconvolution and elemental concentration analysis were done with the software package MultiPak V6.0A (Physical Electronics, Inc.). A pretreatment system, equipped with a separate gas-handling system, attached to the XPS system, allowed in situ sample transfer between each cycle of pretreatment (up to atmospheric pressures) and the main XPS UHV chamber.

3. Results

3.1. Nanofabrication

The main steps in the fabrication of Pt particles on alumina or ceria supports are depicted in Fig. 1 and have previously been described and characterized in more detail [11]. Thin films (20–50 nm) of either alumina or ceria were evaporated onto oxidized silicon wafers, followed by the evaporation of a Pt film (14–20 nm). The Pt surfaces were subsequently treated with water solutions of poly(diallyldimethylammonium) (PDDA), poly(sodium 4-styrenesulfonate) (PSS), and aluminum chloride hydroxide (ACH) to form a thin double layer of polyions with adsorbed

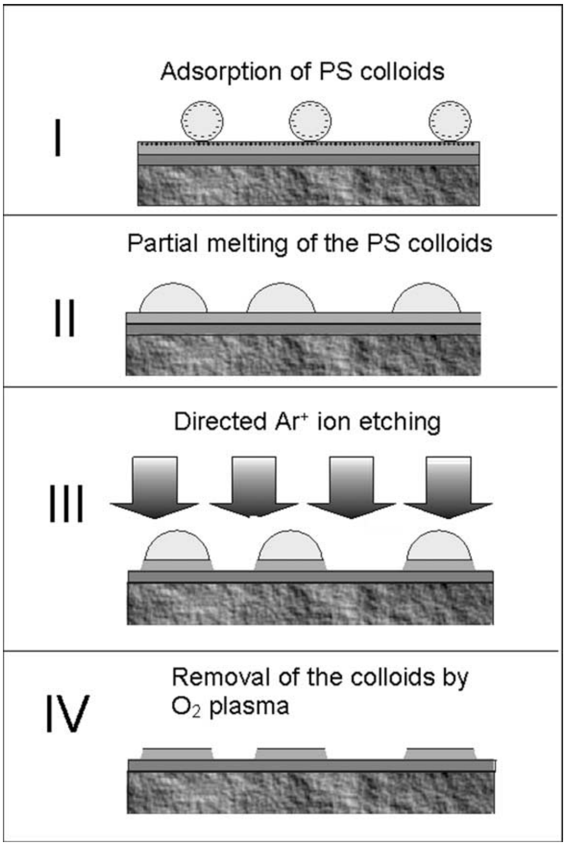

Fig. 1. The colloidal lithography fabrication procedure for flat Pt particles: (I) deposition of a ceria or an alumina film, deposition of Pt film on a silicon wafer, followed by self-assembled adsorption of polystyrene colloidal particles; (II) melting of the colloids; (III) removal of uncovered Pt by directed Ar^+ etching; and finally (IV) removal of the polystyrene particles by oxygen plasma.

aluminum ions, which gives the surface a net positive charge. A water suspension of 0.1 w/w 107-nm PS colloids with 0 or 0.2 mM dissolved NaCl was then rapidly poured over the Pt surface to immediately cover the whole surface with the colloidal suspension, after which the sample was rinsed in water and blown dry with nitrogen gas. The negatively charged PS particles adsorb onto the positively charged Pt surface with a land and stick behavior and the charge of the PS particles prevent them from adsorbing closer to a neighboring particle than a certain minimum distance. The adsorbed PS colloids were melted to hemispheres by placing the silicon substrate on a hot plate for 2 min at 112 °C. This step is included to prevent Pt from being adsorbed underneath the PS particles during Ar^+, which leads to the formation of nonflat Pt particles. The melting leads to an increase of the PS particle diameter from 107 to ∼ 130 nm. To develop the pattern formed by the colloidal particles, directed Ar^+ sputtering (etching) was applied. In a previous study [11], the Ar^+ etching was continued up to the point when all Pt not shadowed by the PS hemispheres was removed and the ceria layer was reached. In the present study the Ar^+ etching time was extended (6 min compared to 2 min), which is longer than what was necessary to etch through the Pt layer (Fig. 2). Thus, by utilizing the fact that the polystyrene is etched at a rate of ∼ 7 nm/min with the parameters used here (500 V, 0.2 mA/cm^2), while Pt is etched at ca. twice that rate (∼ 13 nm/min), the polystyrene particles were etched down to 40 nm, which resulted in Pt dots smaller than the original PS particle (Fig. 3) after the PS removal step. A higher etching speed for ceria (6 nm/min) compared to alumina (3 nm/min) in combination with the thicker alumina layer resulted in the ceria layer being totally etched through down to the underlying silica layer, whereas the alumina layer was still a homogeneous film after the etching, as seen in Figs. 3B and 3C. The samples were subsequently exposed to oxygen plasma to remove residual contaminants and finally cut to pieces of the desired size with a diamond saw. In the present study, no H_2 reduction step to reduce the plasma-oxidized catalysts was included in the preparation procedure. The resulting Pt/ceria sample consisted of 40-nm Pt dots on 100-nm ceria particles and the Pt/alumina sample of 40-nm Pt dots on an alumina film, each with an interparticle separation of ≈ 220 nm (Fig. 4). The projected Pt coverage was 4% in both cases (corresponding to a particle density of 3×10^9 cm^{-2}), and the dispersion was about 2.7% (fraction of Pt surface atoms) as obtained from the SEM image analysis, i.e., typical for a sintered Pt catalyst. It should be noted that the size of the particles can readily be made even smaller and the lower limit is in principle only limited by how monodisperse the original PS colloids are. We refer the reader to Ref. [11] to a more thorough investigation of the chemical state of the model catalyst after each of the preparation steps outlined above. In essence, adopting appropriate precautions, no traces of contamination inherent from the fabrication process is present on the final model catalyst.

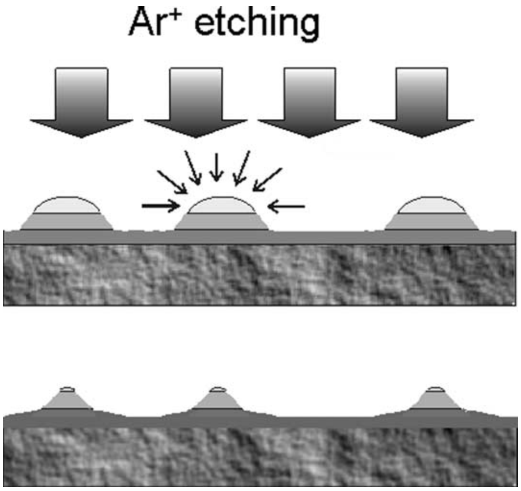

Fig. 2. By utilizing extended Ar^+ etching times, the adsorbed polystyrene particles (melted to hemispheres) are shrunk during the etching, resulting in Pt dots smaller than the original polystyrene particle.

3.2. XPS

XPS spectra were recorded for 40-nm Pt/ceria and Pt/alumina samples. The Pt-oxidation state of each sample,

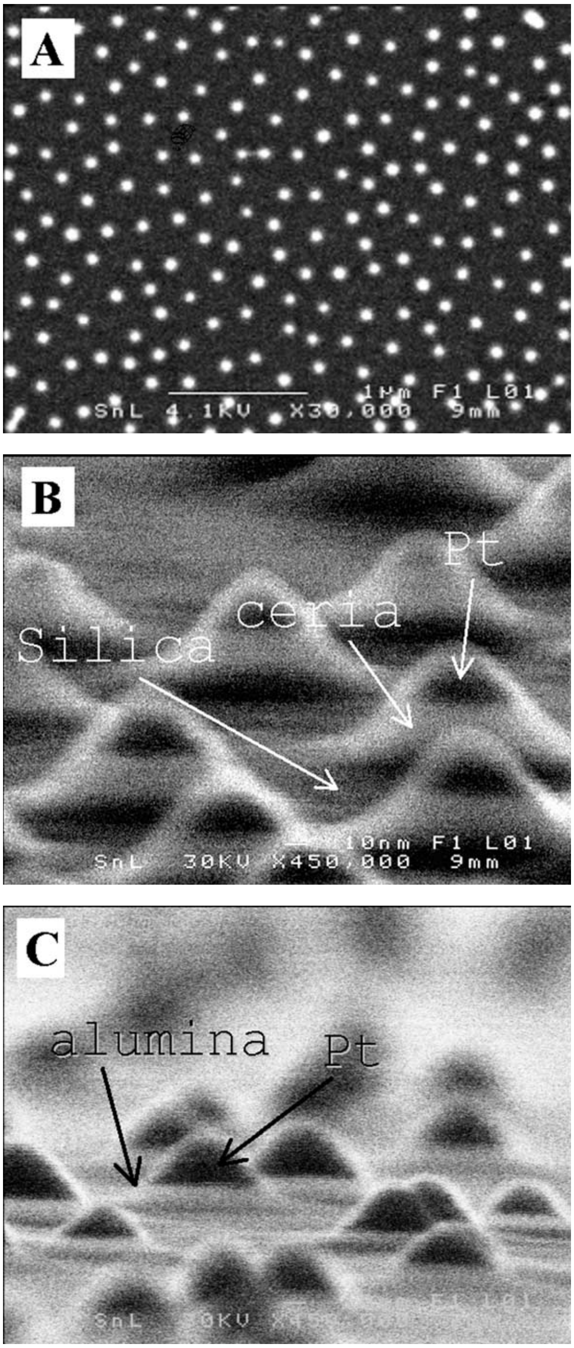

Fig. 3. SEM micrographs depicting 40-nm Pt dots on ceria or alumina made by prolonged Ar^+ etching of the 130-nm colloidal mask. (A) Top view of the resulting Pt/ceria sample. (B) Inclined view of the Pt/ceria sample showing 40-nm Pt dots situated on top of 100-nm ceria particles on silica. (C) Inclined view of the Pt/alumina sample showing 40-nm Pt dots situated on an alumina film. The elevation in the alumina in a zone around the Pt particles reveals the size of the original 130-nm polystyrene hemisphere.

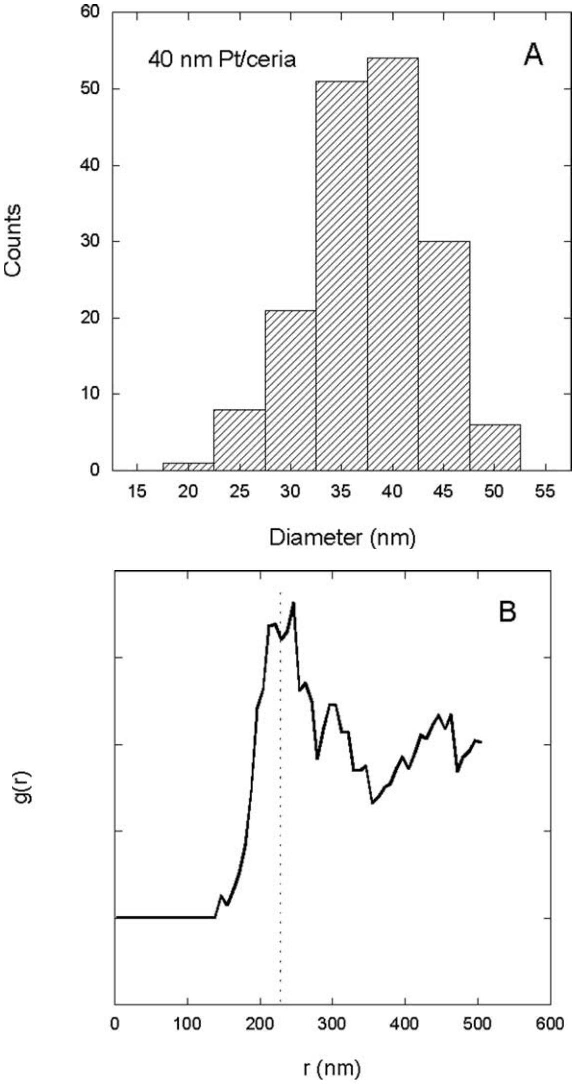

Fig. 4. (A) The particle size distribution and (B) radial distribution function, $g(r)$, for the Pt/ceria model catalyst shown in Fig. 3. The results for Pt/alumina are similar.

i.e., the fractions of Pt, PtO, and PtO_2, was obtained by deconvolution of the XPS Pt $4f$ peaks using iterated Shirley background subtraction and Gauss–Lorentz peak fitting. Following previous studies [25], the following constraints were made to quantify the spectra: (1) the separation between the 5/2 and 7/2 doublets of the Pt, PtO, and PtO_2 peaks was restricted, (2) the separation between Pt and PtO and the separation between Pt and PtO_2 were restricted, and (3) the area ratios between the Pt, PtO, and PtO_2 $7/2 : 5/2$ peaks were fixed. For the aged 40-nm Pt/ceria catalysts, the XPS signal was very weak, which complicated the quantitative analysis. We adopted a procedure in which the peak positions of the various Pt mixed states was set fixed, based on a routine where the overall error (χ^2 fit) between the peak deconvolution and all experimental spectra was minimized. The error in the absolute binding energies for the Pt and PtO_x states is estimated to be ±0.25 eV in this latter case. The relative error in the binding energies is estimated to be accurate to within 0.1 eV.

3.2.1. *Fresh samples*

We have previously shown that the Pt particles become deeply oxidized during the O_2 plasma treatment in the last fabrication step (PS removal) [11]. The Pt can, however,

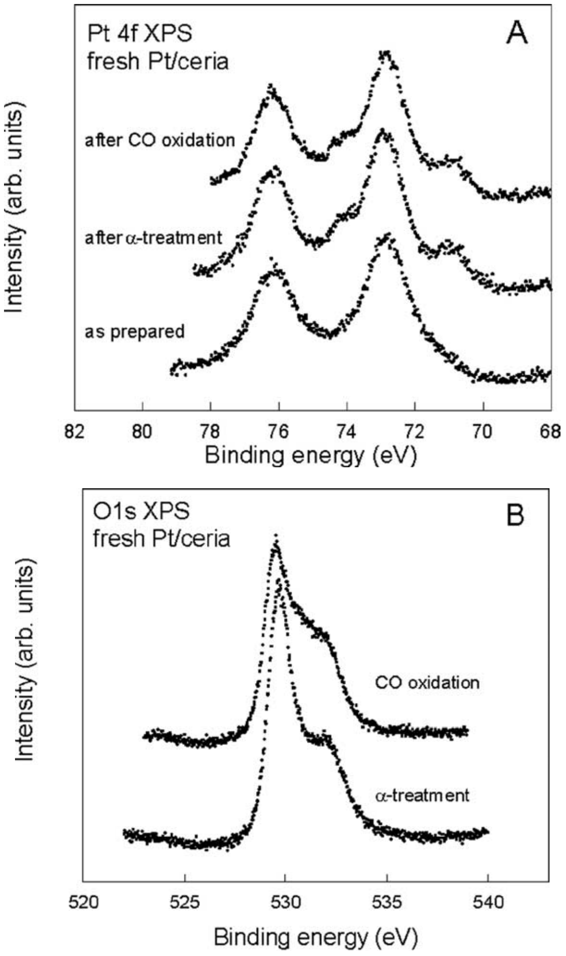

Fig. 5. (A) XPS showing the Pt $4f$ spectra measured on fresh (as prepared) 40-nm Pt/ceria and Pt/ceria subjected to various in situ pretreatments. (B) The corresponding O $1s$ XPS spectra following the same pretreatments.

readily be reduced back to the metallic state either by adding an H_2 plasma treatment step in the fabrication process or by simple in situ reduction or annealing prior to reactivity measurements [11]. Ceria, however, stabilizes Pt oxide, and a significant amount of mainly PtO remains (ca. 30% PtO_2, and 1–2% PtO_2) even after an H_2 plasma treatment or vacuum annealing [11]. In Fig. 5A the Pt $4f$ XPS spectra are shown. It is seen that an H_2/O_2 (α-) pretreatment (1 h at $T = 573$ K, $\alpha \equiv P_{H_2}/(P_{H_2} + P_{O_2}) = 0.33$, 0.5% H_2 diluted in Ar) or CO oxidation (1 h at $T = 593$ K, $\beta \equiv P_{CO}/(P_{CO} + P_{O_2}) = 0.1$) is not sufficient to reduce the 40-nm Pt/ceria sample. About 80% of the Pt remains in the oxidic state after these initial pretreatments (Table 1). The corresponding O $1s$ XPS spectra shown in Fig. 5B show that the intensity of the higher binding energy feature increases substantially after CO oxidation compared to the fresh and α-treated samples. The latter observation is in agreement with previous results, which indicate the presence of carbonate on the surface after CO oxidation [16]. In contrast to Pt/ceria, Pt on alumina transforms readily, as expected [19], to metallic Pt after any of the pretreatments discussed above. The quantification of the Pt state for the Pt/alumina samples is, however, complicated by the Al $2p$ peak (which is the dominant peak in this binding energy region). The Al $2p$ peak overlaps with the Pt $4f$ peaks, and inspection of the Pt $4d$ XPS peaks is also necessary.

3.2.2. Aged samples

In Fig. 6 the XPS spectra are shown for a 40-nm Pt/ceria sample subjected to ca. 100 h reactions and pretreatments. Table 3 in Section 3.4 presents the complete reaction history of the sample (except that the stoichiometric CO oxidation was replaced by CO oxidation in a $\beta = 0.1$ gas mixture). Inspecting the Pt $4f$ binding energy region, the following features are evident from Fig. 6A: (i) The Pt particles contain a large amount of PtO_x, which is evident by the appearance of the peaks at observed at ~ 77 eV (Pt(IV) $4f_{5/2}$) and ~ 72.50 (Pt(II) $4f_{5/2}$), respectively (Table 2). (ii) The Pt $4f$ peak intensity is significantly reduced, which is reflected in the Pt/Ce concentration ratio, which decreases from ca. 0.034 for the fresh sample to ca. 0.022 for the aged sample. Finally (iii), a slight change in the peak separation of the Pt and PtO_x peaks is observed, where, e.g., the Pt–PtO

Table 1
Effect of pretreatment: compilation of the XPS analysis obtained from the fresh Pt/ceria sample in Fig. 3

Pretreatment	Pt		PtO		PtO_2		
	$4f_{7/2}$	$4f_{5/2}$	$4f_{7/2}$	$4f_{5/2}$	$4f_{7/2}$	$4f_{5/2}$	
As prepared	70.95	74.15	72.75	76.00	74.10	77.30	BE [eV]
	1.25	1.25	1.60	1.60	1.50	1.50	FWHM [eV]
	11%		84%		5%		Area
After α-treatment (1 h at $T = 573$ K, $\alpha = 0.33$)	70.95	74.15	72.75	76.00	74.10	77.30	BE [eV]
	1.25	1.25	1.60	1.60	1.50	1.55	FWHM [eV]
	19%		75%		6%		Area
After CO oxidation (1 h at $T = 593$ K, $\beta = 0.1$)	70.95	74.15	72.75	76.00	74.10	77.30	BE [eV]
	1.28	1.28	1.60	1.60	1.50	1.55	FWHM [eV]
	21%		77%		2%		Area

The binding energy (BE) and the full width at half-maximum (FWHM) are obtained from the peak deconvolution procedures described in the text. The area is the background-subtracted integrated peak area.

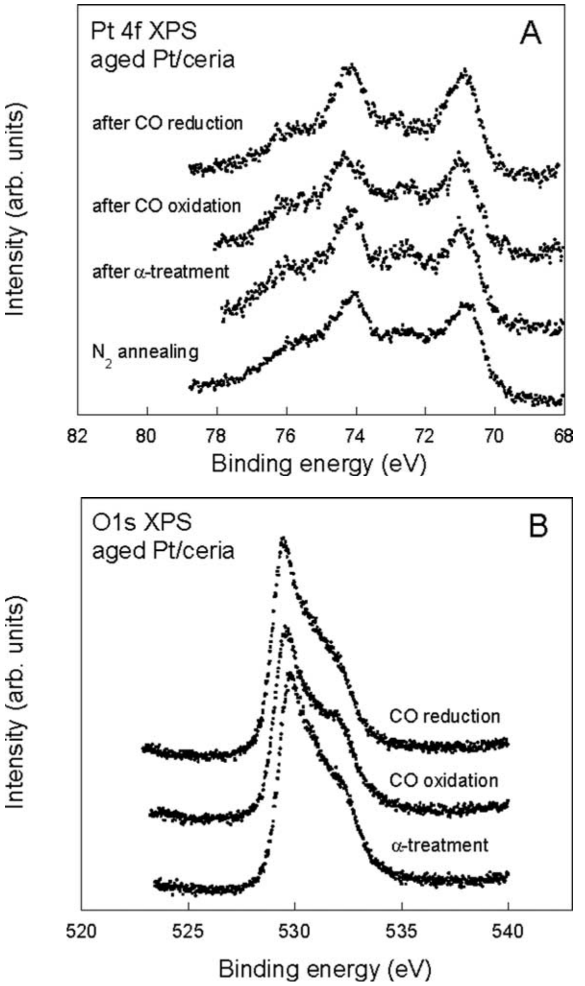

Fig. 6. (A) The Pt $4f$ XPS spectra obtained from an aged Pt/ceria subjected to the history presented in Table 3. (B) The corresponding O $1s$ spectra. The XPS was performed on the same sample as depicted in Fig. 12A.

peak separations decrease by ca. 0.35 eV (see Table 2). The corresponding O $1s$ spectra depicted in Fig. 6B indicate that the influence of various pretreatments is substantially reduced compared to the fresh Pt/ceria sample. A slight increase of the higher binding energy peak intensity after CO oxidation is observed and is in analogy with the fresh sample attributed to carbonate formation. The much higher intensity of the high-binding-energy spectral feature following either CO reduction or an α-treatment is attributed to an increasing amount of $O^{\delta-}$ species [16].

3.3. *Effect of pretreatments on the reactivity*

3.3.1. *O_2 plasma*

As we have previously shown, Pt becomes heavily oxidized during the final oxygen-plasma cleaning step in the preparation. It is therefore important to determine the influence of the plasma cleaning on the CO oxidation behavior. In Fig. 7 is shown the CO to CO_2 conversion as a function of temperature for Pt/ceria before and after an O_2 plasma treatment. The O_2 plasma was performed on a sample that had been "activated" in situ (i.e., oxidized/reduced 1 h at 673 K followed by repeated CO oxidation cycles in a $\beta = 0.1$ gas mixture up to 573 K). An up-shift of T_{50} (the temperature at which 50% of maximum conversion reached) is observed in the first cycle after O_2 plasma treatment, which is accompanied by an up-shift of the apparent activation energy, E_a^*, at $< 10\%$ conversion. A bend in the slope of the Arrhenius plot can be observed and exists (to a lesser extent) also after a CO oxidation cycle followed by a CO reduction. After repeated CO oxidation cycles E_a^* approaches the value prior to the O_2 plasma treatment. We attribute the bend in the slope of the Arrhenius plot to the decomposition of the oxide. The reduction process continues over several CO oxidation and/or

Table 2
Effect of pretreatment: compilation of the XPS analysis obtained from the aged Pt/ceria sample in Fig. 13

Pretreatment	Pt		PtO		PtO_2		
	$4f_{7/2}$	$4f_{5/2}$	$4f_{7/2}$	$4f_{5/2}$	$4f_{7/2}$	$4f_{5/2}$	
After 1 h annealing in N_2	70.95	74.15	72.40	75.60	74.10	77.30	BE [eV]
	1.28	1.28	1.60	1.60	1.50	1.55	FWHM [eV]
	47%		37%		16%		Area
After α-treatment (1 h at $T = 573$ K, $\alpha = 0.33$)	70.95	74.15	72.40	75.60	74.10	77.30	BE [eV]
	1.28	1.28	1.60	1.60	1.50	1.50	FWHM [eV]
	41%		45%		14%		Area
After CO oxidation (1 h at $T = 593$ K, $\beta = 0.1$)	70.95	74.15	72.40	75.60	74.10	77.30	BE [eV]
	1.28	1.28	1.60	1.60	1.50	1.55	FWHM [eV]
	47%		38%		15%		Area
After reduction in CO (1 h at $T = 673$ K in 0.5% CO diluted in Ar)	70.95	74.15	72.40	75.60	74.10	77.30	BE [eV]
	1.28	1.28	1.60	1.60	1.50	1.55	FWHM [eV]
	58%		27%		15%		Area

The binding energy (BE) and the full width at half-maximum (FWHM) are obtained from the peak deconvolution procedures described in the text. The area is the background-subtracted integrated peak area.

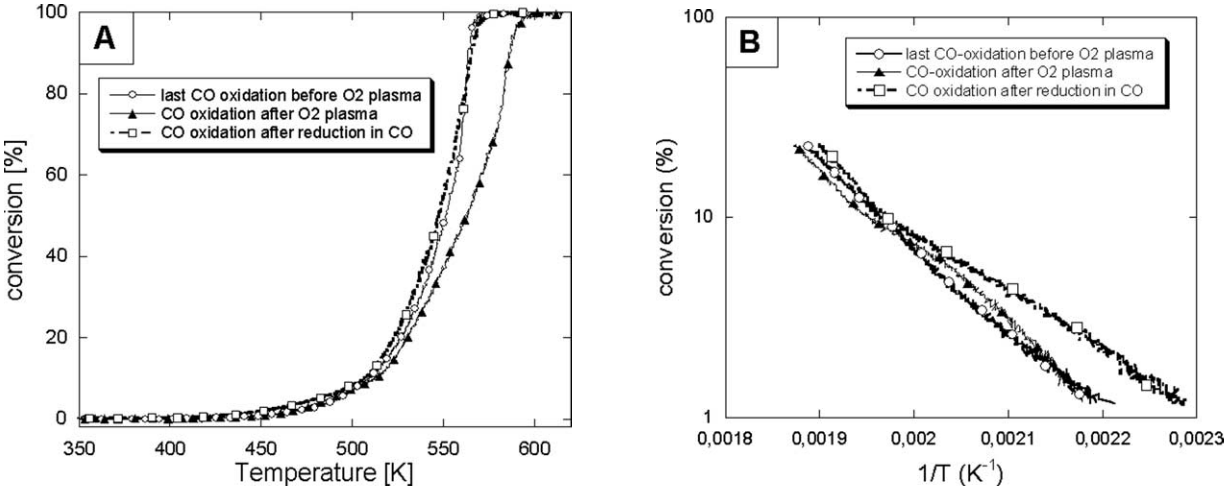

Fig. 7. (A) The CO → CO_2 conversion curves obtained on a 40-nm Pt/ceria catalyst before and after an O_2 plasma treatment. (B) The corresponding Arrhenius plots. The heating ramp was 10 K/min, the CO concentration was 0.5%, and the gas mixture was fixed at $\beta = 0.1$.

reduction cycles in qualitative agreement with the XPS result (Fig. 6).

3.3.2. *Reduction in CO and H_2*

The reduction of the 40-nm Pt/alumina and Pt/ceria samples results in very different CO oxidation response. Fig. 8A shows the result after reduction in 0.5% CO for 1 h at 673 K for 40-nm Pt/ceria. The first cycle after reduction has a broadened conversion curve accompanied by a high T_{50}. The conversion curves shift gradually down, while the widths simultaneously decrease after repeated CO oxidation cycles. On fresh Pt/ceria E_a^* increases after prolonged CO reduction (Fig. 8C). The estimate of E_a^* is, however, complicated due to the irregular conversion curve, which is particularly pronounced directly after the reduction step. The value of E_a^* (given in arbitrary units—see Section 4; the conversion factor is E_a^* (kJ/mol) $= 8 \times E_a^*$ (arbitrary units)) is therefore determined as an average at $< 15\%$ conversion (at very low conversion E_a^* directly after reduction is in fact lowered compared to the catalyst prior to reduction). It is known that CO may dissociate on Pt/ceria and even embed the particles in carbonaceous layers at sufficiently high temperatures, and that this affects the reactivity (e.g., site blocking) [13,15,18]. The CO reduction performed here does not, however, completely deactivate the catalyst, as previously reported [17], even though the activity of the catalyst is difficult to recover and it is back to a highly active state only after additional α-treatments. To explore this effect further and to test if carbon deposition is important, we reduced a 40-nm Pt/ceria sample in H_2 (4% at 673 K for 1 h). As is evident from Fig. 8B, the CO conversion curve broadens significantly more after H_2 reduction compared to CO reduction. The T_{50}, however, shifts down, but approaches the CO conversion curve prior to reduction already after the second CO oxidation cycle. In contrast to CO reduction, the H_2 reduction results in a pronounced decrease of E_a^* (Fig. 8C). The main effect of the C residues on the conversion curve is therefore not the broadening (which is more pronounced after H_2 reduction), but the up-shift of E_a^* and T_{50} and the long-term "memory" effect. Instead we attribute the broadening of the conversion curve to a reduction of ceria, which is known to be most pronounced after H_2 reduction [26]. The up-shift of T_{50} in the case of CO reduction is consequently attributed to CO dissociation and carbon site blocking on the Pt particles. The greater reactivity following H_2 reduction is in good agreement with previous findings, where it is found that the degree of reduction is highest after H_2 reduction, much higher than after CO reduction [26], and that the chemical state of the ceria catalyst greatly affects the reactivity; a reduced catalyst is suggested to promote the catalytic activity [27]. The negative effect of CO reduction on the catalytic activity may be associated with the long-time CO reduction treatment employed here causing C deposition on the catalyst, since the improved reactivity of reduced ceria also is manifested in improved CO dissociation activity [26]. We have, however, as yet not performed a detailed study of the effect of long-term CO reductions. In contrast, the reduction does not affect the CO oxidation behavior on 40-nm Pt/alumina significantly and does not change further upon repeated CO oxidation cycles, in agreement with previous studies [19]. In Fig. 9 are depicted the first two CO oxidation cycles following a CO reduction (0.5% CO at 673 K for 1 h). The result from the H_2 reduction is similar.

3.3.3. *H_2/O_2 pretreatment*

3.3.3.1. Influence on reactivity A common way to clean Pt model catalysts by chemical means is to pretreat them in (nonexplosive) mixtures of H_2 and O_2 (a so-called α-treatment) [14,28,29]. This has been shown to work satisfactorily on Pt/ceria catalysts prepared by electron beam lithography, where high-temperature treatments must be avoided. We performed a series of α-treatments ($\alpha = 0.33$ at 573 K for 1 h) and in between treatments performed a

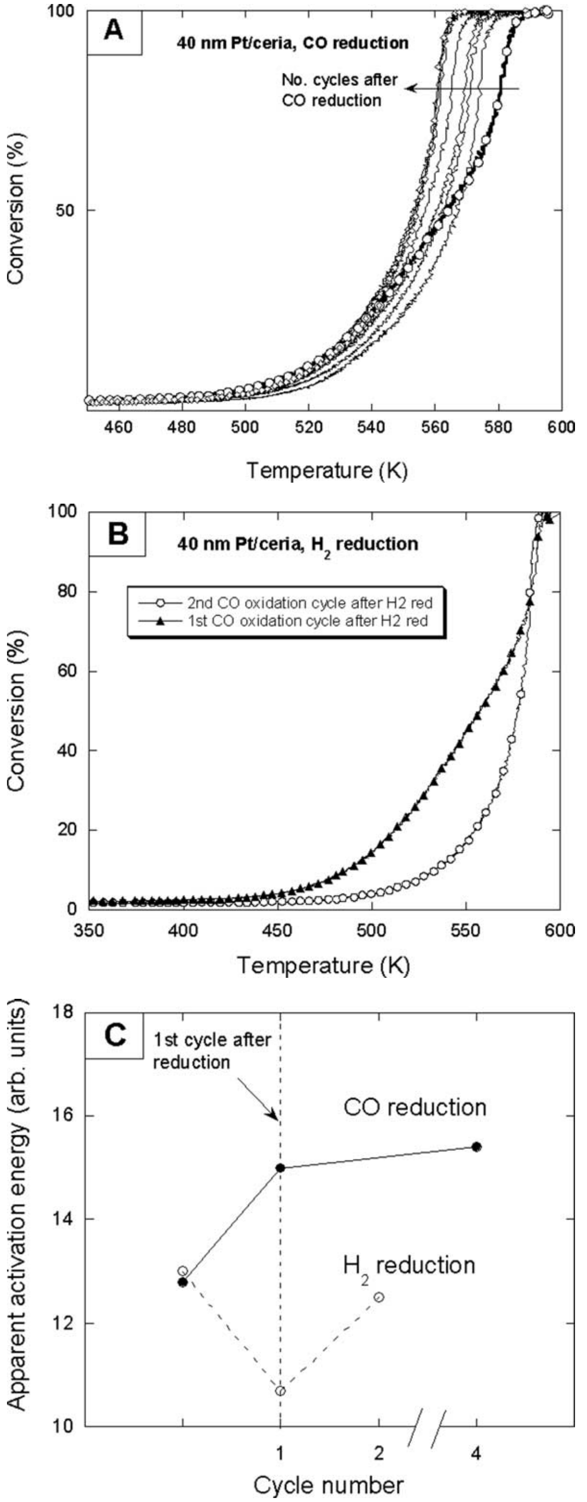

Fig. 8. (A) The effect of prolonged CO reduction (0.5% CO diluted in Ar at 673 K for 1 h) on the CO → CO_2 conversion curves for 40-nm Pt/ceria. (B) The corresponding conversion curves obtained after a H_2 reduction (4% H_2 diluted in Ar at 673 K for 1 h). (C) The apparent activation energy obtained from A and B. The heating ramp in the CO oxidation experiments was 10 K/min, the CO concentration was 0.5% and the gas mixture was fixed at $\beta = 0.1$.

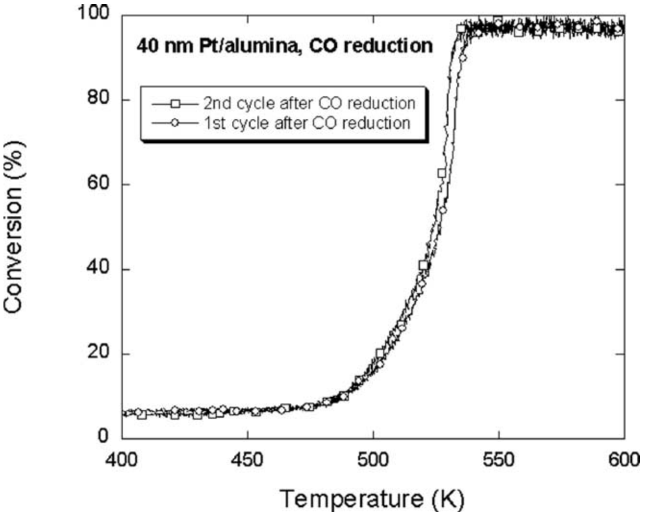

Fig. 9. The effect of CO reduction (0.5% CO diluted in Ar at 673 K for 1 h) on the CO → CO_2 conversion curves on 40-nm Pt/alumina. The heating ramp in the CO oxidation experiments was 10 K/min, the CO concentration was 0.5%, and the gas mixture was fixed at $\beta = 0.1$.

series of CO oxidation cycles. The result confirms the picture that α-treatment "cleans" the Pt/ceria samples efficiently [14,24]. A slight initial increase of T_{50} and E_a^* suggests, however, a weak inhibition (by hydroxyl groups [14]), which after a few CO oxidation cycles readily is removed (Fig. 10A). On the other hand, the catalytic activity of Pt/alumina catalysts is significantly affected by an α-treatment (Fig. 10B). Several subsequent CO oxidation cycles are required to obtain a "typical" conversion curve for an activated catalyst (with a T_{50} in the same range as in Fig. 9).

3.3.3.2. Temperature programmed desorption A series of CO-TPD measurements were performed to elucidate in more detail the effect of the α-treatment on the Pt/alumina model catalysts. Two samples with a 1 cm^2 total surface area were studied: (1) A 107-nm Pt/alumina sample with a particle density of $8.3 \times 10^{10}/cm^2$, which corresponds to a projected Pt surface coverage of 30%. A higher Pt loading was used to enhance the CO-TPD signal; (2) A 30-nm-thick platinum film evaporated on a 30-nm-thick alumina film. To further enhance the effect of the α-treatment, each sample was pretreated at 673 K for 10 h in a mixture of 0.5% H_2 and 1% O_2 diluted in Ar ($\alpha = 0.33$) at 1 bar. The samples were subsequently annealed in vacuo to 673 K. The samples were exposed to between 6 and 600 L of CO in vacuo. All exposures were done at 300 K, after which the temperature was ramped to 673 K with a heating rate of 15 K/min. In Fig. 11 the TPD spectra from the Pt film and the Pt/alumina sample are shown. Two TPD peaks are seen for the Pt film at ∼ 360 and ∼ 420 K. With decreasing CO exposure the TPD peak at the lower temperature vanishes, and only the high-temperature TPD peak remains. The position of the CO desorption peak from the Pt film is about 50 K lower than in previous reports [1,30]. This can in part be

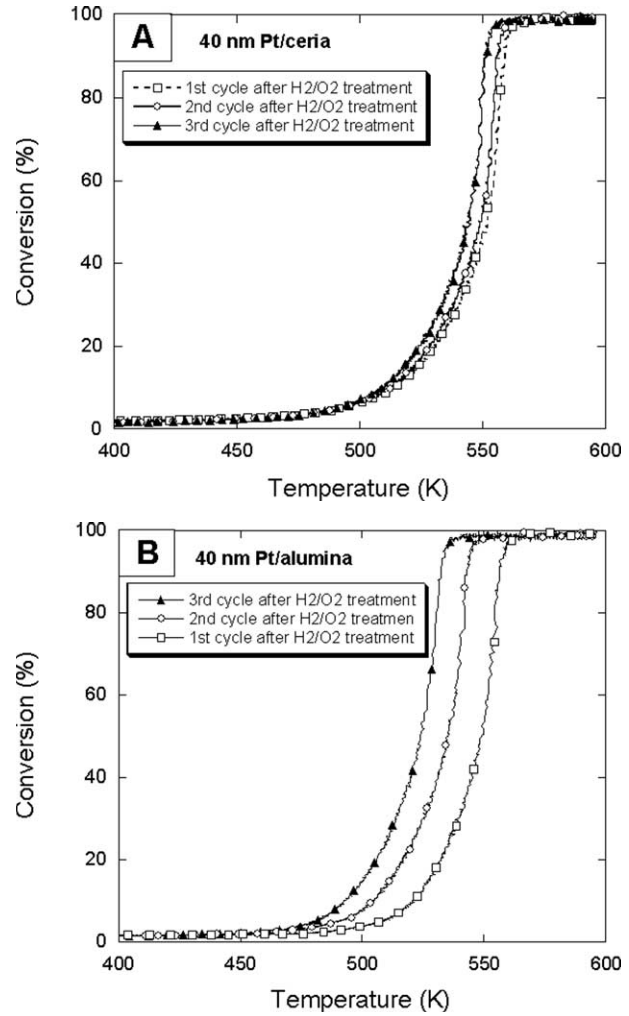

Fig. 10. The effect of H_2/O_2 pretreatments ($\alpha = 0.33$, 0.5% H_2 diluted in Ar at 573 K for 1 h) on the $CO \rightarrow CO_2$ conversion curves on 40-nm Pt/ceria (A) and 40-nm Pt/alumina (B), respectively. The heating ramp in the CO oxidation experiments was 10 K/min, the CO concentration was 0.5%, and the gas mixture was fixed at $\beta = 0.1$.

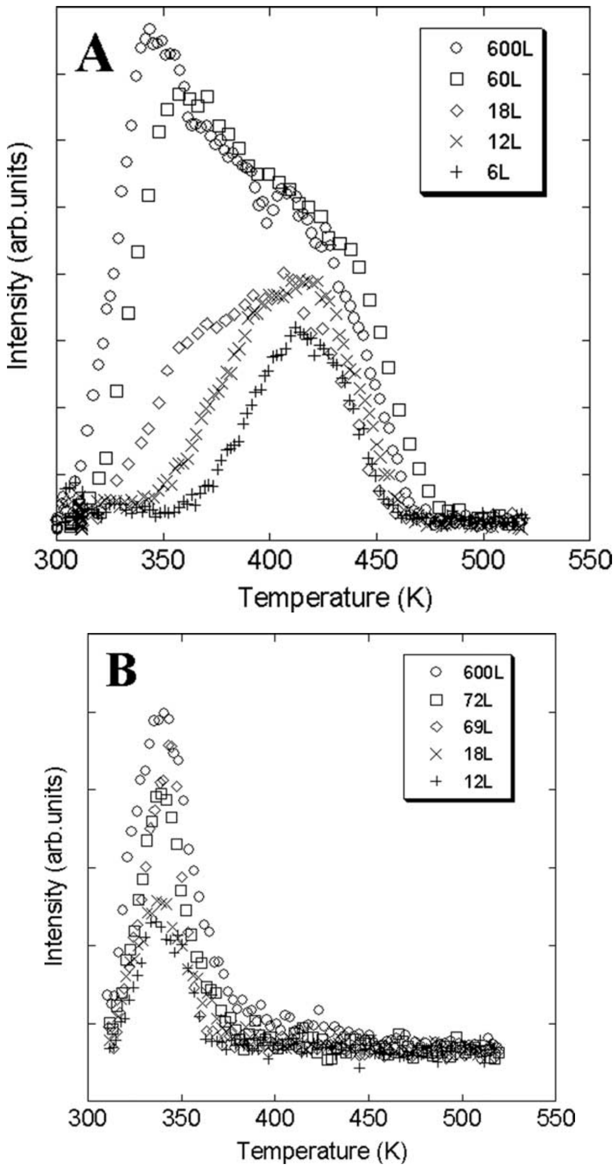

Fig. 11. The CO desorption vs temperature at various CO exposures obtained from (A) a 30-nm thick Pt film grown on alumina and (B) a 107-nm Pt/alumina. The heating rate was 15 K/min.

explained by the comparatively low heating rate employed here (0.25 K/s, which is 1 order of magnitude slower than most vacuum TPD experiments), but also to imperfect contact between the thermocouple pressed to the front sample surface and the thermal inertia in the system caused by the Macor piece pressing the thermocouple against the surface. The qualitative shape of the TPD curves from the Pt film is, however, in good agreement with literature data [1,30]. The CO-TPD spectra from the 107-nm Pt/alumina sample show different qualitative behavior. All CO desorbs at ∼ 360 K, even at the low CO exposures, corresponding to the position of the low-temperature desorption peak for the Pt film. From Fig. 11 we estimate that the total number of adsorbed CO molecules (normalized to the geometric Pt surface area) is ca. four times lower on the nanofabricated sample than on the film. Previous studies of CO desorption from vapor-deposited Pt clusters on alumina have shown the opposite trend, compared to our result, for very small Pt clusters ($d < 5$ nm), i.e., redistribution of the TPD peaks toward higher temperatures [30]. In another study of vapor-deposited Pt clusters on ultrathin alumina layers [31] it was observed that most CO desorbed in a broad peak ∼ 420 K for large Pt clusters with weak shoulders at lower and higher temperatures, whereas the TPD peak shifts to higher temperatures for smaller clusters (smaller Pt coverages). On the smaller clusters a low-temperature peak between 150 and 200 K was also observed. In this latter study it was also observed that the TPD area decreased significantly between the first and second TPD experiments and in the latter case only exhibited a broad, single peak at ∼ 400 K. The latter observation has been (in part) attributed to Pt metal atom diffusion through the thin oxide layer [32]. Due to the quite large Pt particles used in this study (107 nm) we should

Table 3
Survey of the microflow reactor measurements performed on the Pt/ceria samples shown in Fig. 13A

Pretreatment	t (min)	T (K)	T_{50} (K)[a]	E_a^* (arb. units)[a]	Cycle no. in Fig. 12	Total no. cycles[b]
α-treatment[c]	60	573	559	13.4	1	13
CO-oxidation[d]	20	593	537	12.8	2	15
CO-oxidation	75	593	557	12.8	3	17
Reduction in 0.5% CO	60	673			–	
CO-oxidation	100	593	556	15.0	4	25
CO-oxidation	500	593	556	15.4	5	28
α-treatment	120	573			–	
CO-oxidation	20	593	543	13.4	–	
CO-oxidation	70	593	542	14.0	6	34
α-treatment/CO oxidation	60/100	573/593	536	13.0	7	48
α-treatment/CO oxidation	60/20	573/593	537	12.0	8	55
Reduction in 0.5% CO	60	673				
CO-oxidation	60	593	542	12.5	9	59
α-treatment	90	573			–	
CO-oxidation	60	593	546	12.6	10	64
CO-oxidation ($\beta = 0.66$, 0.02% CO)	300	673			–	
CO-oxidation	30	593	543	16.0	11	69
Reduction in 2% CO/CO-oxidation	480/100	673/593	552	17.1	12	75

[a] After each pretreatment a CO oxidation experiment (ramp rate 10 K/min in a $\beta = 0.1$ gas mixtures) was performed, yielding T_{50} and E_a^*.

[b] The total number of cycles indicate the number of CO oxidation cycles (ramp rate 10 K/min in a $\beta = 0.1$ gas mixtures) the sample has been subjected to.

[c] $\alpha = 0.33$ ($H_2 = 0.5\%$).

[d] $\beta = 0.1$ ($CO = 0.5\%$).

not expect to see a size effect as observed for very small (a few nm) Pt particles. Our CO-TPD spectra of 107-nm Pt/alumina resemble those obtained for larger Pt clusters in the study above [31], with the exception that we do not distinguish any structures in the TPD spectra at higher desorption temperatures.

3.4. *Reactivity of aged model catalysts*

In Table 3, the history of a 40-nm Pt/ceria sample is described, which includes 75 CO oxidation cycles and ca. 100 h of either CO oxidation (460–600 K), α-treatments ($\alpha = 0.33$ at 573 K), or CO reductions (673 K). The corresponding T_{50} and E_a^* are shown in Fig. 12A. As described above, extended reductions in CO cause up-shift of both T_{50} and E_a^* (cycle 4 in Fig. 12A). A lower value of T_{50} and E_a^* can, however, be "restored" by α-treatments (cycles 5–7). We also note that extended CO oxidation on a fresh Pt/ceria sample in oxygen excess ($\beta = 0.1$) at 573 K leads to an increase of T_{50}, while E_a^* remains the same. The latter may be associated with carbonate formation (cf. Fig. 5B), which provides a different CO_2 channel with different kinetics (and a different number of active sites; see Section 4). The effect of the pretreatments decreases substantially as a function of cycle number. After a total of > 40 CO oxidation cycles (with intermittent CO reductions and α-treatments), the T_{50} and E_a^* values are not changed significantly, irrespective of pretreatment prior to a CO oxidation run. After performing an extended CO oxidation reaction at stoichiometric gas mixture (5 h at $\beta = 0.66$, 0.02% CO) at 673 K, the shape of the conversion curve changes dramatically, which is particularly evident from an increased E_a^*. The "normal" CO oxidation behavior could not be restored after this pretreatment by repeated α-treatments or repeated oxygen-rich CO oxidation cycles. The latter observation signals that the 40-nm Pt/ceria catalyst particles have been severely altered chemically and/or structurally. In Fig. 12B the corresponding results for 40-nm Pt/alumina are shown. The Pt/alumina system is not sensitive to reduction treatments as described above. Similarly, no "long-term" aging effect was observed as for Pt/ceria. In particular, no dramatic change following a reaction in a stoichiometric gas mixture was observed (not shown). The T_{50} and E_a^* remained approximately the same after the sixth cycle, irrespective of pretreatments (excluding α-treatments, which causes severe changes, as discussed above). A slight up-shift of E_a^* was, however, observed after an oxidation or reduction treatment. The T-hysteresis obtained by measuring the CO conversion when ramping up and down in temperature disappeared after the sixth CO oxidation cycle. The latter observations may be due to mobile Al ions migrating onto the Pt particles and/or the Pt/alumina interface. At present we do not, however, have an unambiguous explanation for these phenomena, and we will not discuss them further here.

3.5. *Particle morphology*

Fig. 13 shows SEM images of aged 40-nm Pt/ceria and Pt/alumina catalysts used in the CO oxidation experiments described above. In Fig. 13A is shown the 40-nm Pt/ceria sample subjected to the history given in Table 3. The original hemispherical particles (Fig. 3B) have reshaped into pillars, which are sticking up from the surface. The underlying 100-nm ceria islands have also changed from a concave to a convex shape. The aspect ratio (height/length) AR is ∼ 1.5

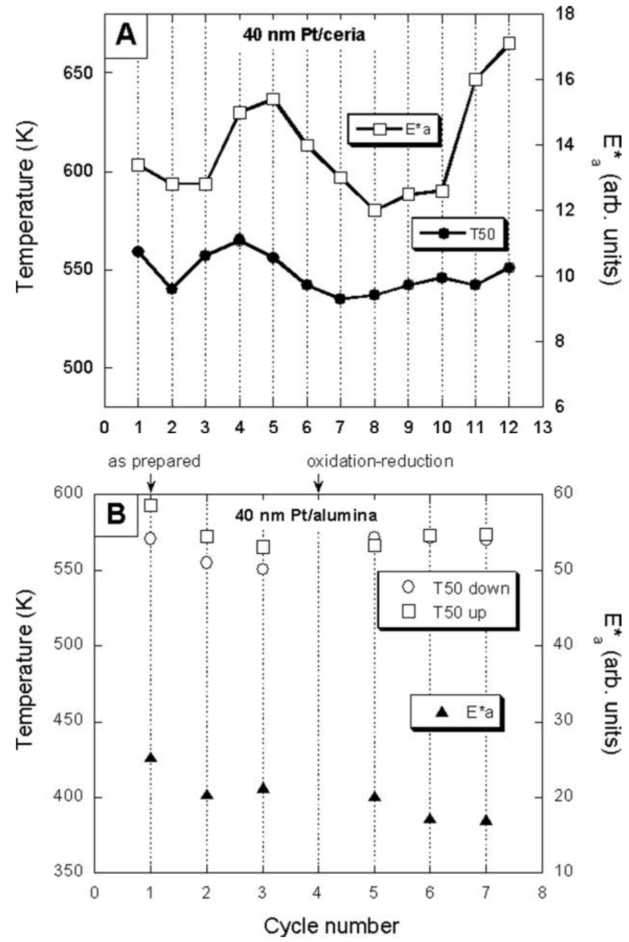

Fig. 12. The effect of aging of the Pt/ceria and Pt/alumina model catalysts on the catalytic activity. (A) T_{50} and E^*_a obtained for Pt/ceria after performing a CO oxidation run following the pretreatments described in Table 3. The cycle number corresponds to the reaction history of the sample given in Table 3. (B) The corresponding results for Pt/alumina. The heating ramp was 10 K/min, the CO concentration was 0.3%, and the gas mixture was fixed at $\beta = 0.1$.

for the pillar structures seen in Fig. 13A, compared to ~ 0.4 for the fresh 40-nm Pt/ceria sample (Fig. 5B). In Fig. 13B is shown a SEM image of a 40-nm Pt/ceria sample, which has been subjected to a history similar to that of the sample in Fig. 13A, except that in this case no CO oxidation was performed at $\beta = 0.66$ (only $\beta = 0.1$). The particles have acquired the same qualitative form as in Fig. 13A, but the pillar structures are much less pronounced and the AR is only ~ 1.0. As expected from the reactivity measurements, the 40-nm Pt/alumina sample does not change the structure as dramatically as Pt/ceria. In Fig. 13C is shown a SEM picture of a 40-nm Pt/alumina sample (the same as depicted in Fig. 3C), subjected to a treatment similar to that for the 40-nm Pt/ceria sample in Fig. 13A (including 5 h CO oxidation at 673 K in a stoichiometric gas mixture). A slight reshaping is observed, with some sharp corners visible in SEM, suggesting faceting; the AR is increased from ~ 0.4 to ~ 0.6 compared to the as prepared Pt/alumina catalyst.

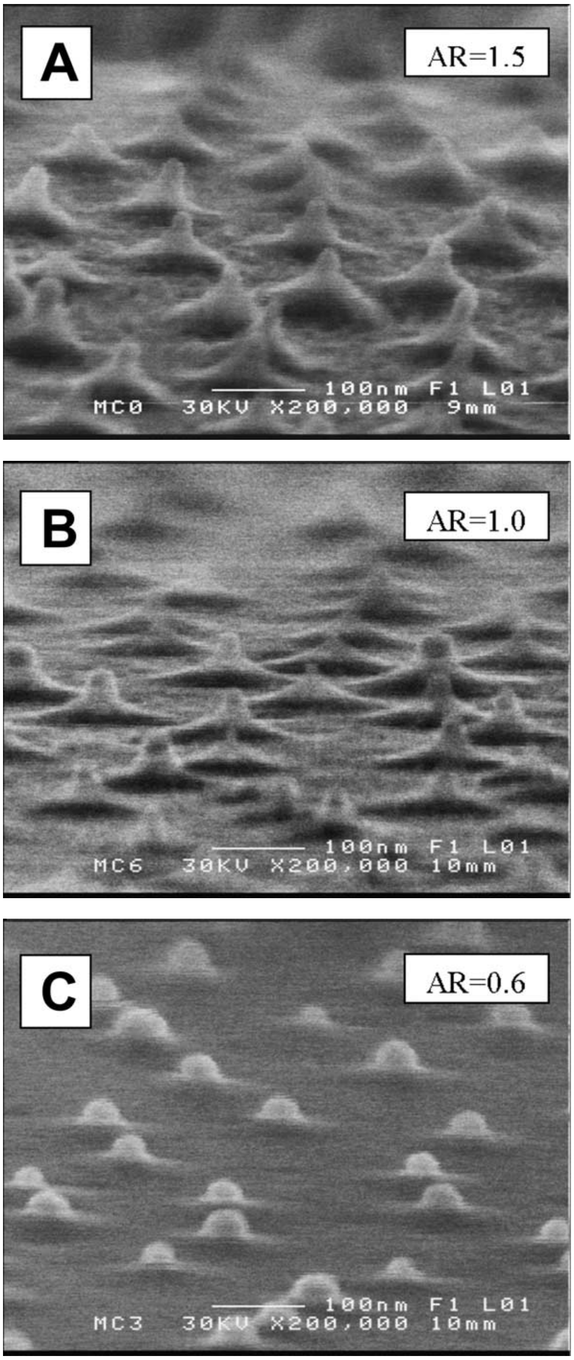

Fig. 13. (A) A SEM image of a 40-nm Pt/ceria sample aged according to the history described in Table 3. (B) A 40-nm Pt/ceria sample aged under similar conditions as in (A), except that no CO oxidation treatments at stoichiometric gas mixtures ($\beta = 0.66$) was performed. (C) A 40-nm Pt/alumina sample exposed to a history similar to that in (A). The aspect ratios (AR) are shown in the upper right corners.

4. Discussion

The overall results for CO oxidation on the 40-nm Pt/alumina and Pt/ceria model catalysts are in good agreement with previous CO oxidation studies on Pt/alumina and Pt/ceria catalysts [12–14,18,19,27,33,34] and show that model catalysts prepared by colloidal lithography can be used with confidence in fundamental catalysis research. The procedure outlined here for making small (40-nm) catalyst particles show that small noble metal particles can be prepared and thus provide samples with particle sizes and dispersions approaching those typically relevant for heterogeneous catalysis application. Hence it is possible to relate microscopic processes occurring on individual particles to macroscopic reaction behavior. The correlation of the reactivity with the structural changes observed in, e.g., Fig. 12 can therefore be correlated with the microscopic information obtained from selected area analysis of a few catalyst particles. The important point is that the macroscopic response is amplified by an ensemble of identical microscopic units present on our model catalysts, which otherwise may be blurred in a heterogeneous system.

In the present study we have studied CO oxidation as a function of temperature by employing a (slow) heating ramp. The information contained in such measurements is complicated by several factors: (i) the measurements are not steady-state measurements (despite the slow heating ramp), and proper activation energies cannot be deduced from an Arrhenius analysis; (ii) the separation of pure kinetic, mass transport, and heat transport effects is nontrivial [29,35]. The CO oxidation, under the conditions described here, can, however, not be characterized by one effective, rate-limiting step described by an Arrhenius-type term, making the interpretation of a simple Arrhenius analysis complicated. Hence extensive theoretical modeling is required to understand CO oxidation even under steady-state conditions [14,29]. Handling of mass transport effects is greatly simplified by employing planar model catalysts and appropriate reactor setups, and complications arising from complex mass transport, pore diffusion, and heat variations are avoided. A simple one-dimensional Fickian diffusion model can therefore be used to describe the mass transport. By employing standard mean-field equations appropriate for CO oxidation at atmospheric conditions on Pt wires and films under such idealized conditions (see our previous studies for details of the simulations [14,29]), we note that the location of T_{50} (up) is indeed very sensitive to the Langmuir–Hinshelwood $CO + O$ reaction step, as expected, but also (to a smaller extent) to the O_2 adsorption kinetics and site blocking. The latter is, e.g., important for CO reduction on Pt/ceria, as discussed above. Similarly, parallel processes (e.g., CO_2 production via carbonate species [16]) may also impede or augment the resulting apparent activation energy differently compared to the measured rate and T_{50}, as seen after extended CO oxidations (Fig. 12A, cycle 3, and Fig. 6B). It is therefore not trivial in this simple model to attribute small shifts observed in the experiments to a particular elementary process, in particular since the results presented here, as well as previous reports (see Ref. [18] and references therein), suggest significant chemical and structural modifications of the catalysts. The apparent activation energy presented here should therefore be used and interpreted with caution. The relative changes of E_a^* does, however, give a measure of the *relative changes of the overall CO oxidation rate* (i.e., not of a particular elementary process). We have therefore deliberately chosen to label E_a^* in arbitrary units.

The most interesting result emerging from this study is the long-term changes of the reactivity and corresponding dramatic reshaping effects of the 40-nm Pt/ceria catalysts seen in SEM and the associated change of the reactivity. A new type of Pt pillar structure is observed to grow out on the aged 40-nm Pt/ceria model catalysts. The shape change of the ceria islands also signals dramatic redistribution of ceria. It is tempting to associate the observed restructuring with a SMSI effect whereby the Pt particles are decorated with Ce or CePt-species. It is well known that Pt interacts strongly with ceria (more strongly than with alumina) [18, 20,33]. The SMSI effect has been studied at the atomic level using HR-TEM [18], but in these studies it was shown that high reduction (H_2) temperatures ($T \sim 1000$ K) are necessary to induce decoration of the Pt particles. The comparatively low temperatures employed in the present study, along with the net oxidizing conditions, suggest that ceria decoration would not occur. An alternative explanation for the decreased reactivity could therefore be crystallization of ceria, which is known to deteriorate the reduction capacity of ceria [16,27,34]. On the other hand, some additional observations, complementing the SEM results, suggest that we indeed have an SMSI effect: (i) The response to the pretreatments described in Table 3 decreases as a function of number of CO oxidation cycles, which is known to be a signature for the (fresh) Pt/ceria system. (ii) The decrease of the Pt $4f$ peak intensity (Pt/Ce concentration ratio) on the aged sample (the sample depicted in Fig. 13A) compared to the fresh sample (Fig. 3) suggests that the particles are encapsulated by, e.g., a ceria layer, thereby lowering the XPS signal. (iii) Deconvolution of the XPS Pt $4f$ spectra indicates a small chemical shift between the fresh and the aged sample, where the different Pt and PtO peak separations (cf. Tables 1 and 2) point to a different chemical environment for the Pt surface atoms. We have, however, no conclusive spectroscopic evidence for the formation of such ceria layers (or PtCe alloy formation) on the particles due to the weak XPS signal on the aged sample. Finally, (iv) E_a^* increases substantially after the stoichiometric CO oxidation pretreatment and is accompanying a dramatic reshaping of Pt/ceria (cf. Figs. 13A and 13B), while the T_{50} value is not affected so much. This is in agreement with previous findings of CeO_2/Pt(111), where a fully covered Pt surface was seen to maintain a high reaction rate, though with a higher E_a^* compared to the bare Pt [16]. Guided by previous studies (see Ref. [18] and references therein), we therefore tentatively conclude that ceria is (partly) encapsulating the Pt particles. The SMSI effect is generally believed to be reversible [18]. We have, however, not pursued a structural analysis following a reoxidation and mild reduction treatment.

The form of the Pt/ceria particles must also include some Pt metal restructuring. The decrease of the Pt–ceria interface length and the corresponding increase of the AR value by almost a factor of 4 imply that the Pt particles themselves reshape into pillars. The pillars are thus not due (solely) to ceria growing out from the particles (which also would result in a much weaker Pt XPS signal). The Pt reshaping is promoted and accentuated by running the CO oxidation at stoichiometry (cf. Figs. 13A and 13B). It is believed that oxygen acts as a surfactant for Pt metal redistribution [36]. A requirement for such a mechanism is that Pt not be oxidized, since this seems to inhibit restructuring, in analogy with the Pt-catalyzed $H_2 + O_2$ reaction [36]. This is accomplished by balancing the $CO + O_2$ reaction to near-stoichiometric conditions ($\beta = 0.66$), so that the fast reaction effectively cleans the surface of adsorbates and simultaneously prevents it from becoming (fully) oxidized. In contrast, the results for the 40-nm Pt/alumina sample show that similar aging, including a $\beta = 0.66$ treatment, does not lead to as a dramatic reshape of the Pt particles. Instead the shapes of the Pt/alumina particles indicate faceting, as is expected for weak metal–support interaction, where the particle shape is mainly governed by the substrate surface energy, γ_s, and the Pt–alumina interface energy, γ_i. The overall form of the particles agree with the Wulff relation, and an AR ratio of ~ 0.6 is about twice the corresponding values observed for small ($\sim$ 3-nm) Pd/Al_2O_3 [37], suggesting a weaker interaction with the support, i.e., a larger effective surface energy, $\gamma^* = \gamma_i - \gamma_s < 0$, and hence a smaller work of adhesion. This is in qualitative agreement with the predicted shapes for alumina-supported Pd having a height/width ratio of about 0.5, and thus a larger effective surface energy [37]. (The reason for the large AR may also in part be due to the amorphous alumina support). Thus comparing the two systems, we conclude that the interface energy is larger for Pt/ceria than for Pt/alumina (as expected).

The Pt/alumina model catalysts show a remarkable sensitivity toward α-treatment, which is seen to deactivate the catalysts and decrease the high-temperature CO desorption peaks as measured by TPD. The relative intensity of the high- and low-temperature CO-TPD peaks is normally interpreted in terms of defect sites on the surface (low-coordinated Pt sites); a rougher surface yields a relatively larger high-temperature (defect-related) desorption peak [1]. The most likely cause of the absence of the high-temperature CO desorption is blocking of the sites corresponding to the high-temperature TPD state by some impurity. CO dissociation is commonly observed not to occur after heating to the moderate temperatures that we use here ($T < 673$ K) [30], while it becomes important after heating to 800 K [31]. We therefore rule out CO-derived C site blocking (which was the case for ceria). Carbon contamination from the nanofabrication process has previously been shown to be negligible [11]. Since the site blocking affects only the Pt/alumina sample and not the Pt film, we conclude that the alumina support must be responsible for site blocking. Lacking any further evidence we propose that Al species (e.g., Al–OH) form on the alumina support/interface during the α-treatment, diffuse onto the Pt particles, and block the high-temperature CO-TPD state (the low-coordinated sites). It is generally observed that electronegative species weaken the Al bonding to the lattice and treatments such as oxychlorination, which is used to redisperse Pt catalysts, readily release Al ions from alumina [38].

5. Conclusions

We have presented a detailed study of the CO oxidation behavior of Pt/alumina and Pt/ceria model catalysts prepared by colloidal lithography. A new method of preparing small Pt particles (40 nm) is presented. The effects of various pretreatments of the Pt/alumina and Pt/ceria model catalysts are in general in good agreement with those observed on corresponding catalysts prepared by different methods, thus validating the nanofabrication method. As a new finding, a site-blocking effect and suppression of the reactivity of Pt/alumina were observed after an α-treatment. Notably, long-time reactions result in substantial restructuring of the 40-nm Pt/ceria catalysts, which has not been observed earlier. The results are attributed to a low-temperature, reaction-induced SMSI effect correlated with a significant change in the catalytic activity.

Acknowledgments

The work in this paper was performed within the Competence Centre for Catalysis, which is financially supported by the Swedish National Energy Administration and the following member companies: AB Volvo, Johnson Matthey-CSD, Saab Automobile AB, Perstorp AB, MTC AB, Eka Chemicals, and Swedish Space Corporation.

References

[1] C.R. Henry, Surf. Sci. Rep. 31 (1998) 235.
[2] D.R. Rainer, C. Xu, D.W. Goodman, J. Mol. Catal. A Chem. 119 (1997) 307.
[3] M. Baumer, J. Libuda, A. Sandell, H.J. Freund, G. Graw, T. Bertrams, H. Neddermeyer, Ber. Bunsenges. Phys. Chem. Chem. Phys. 99 (1995) 1381.
[4] H. Poppa, Catal. Rev. Sci. Eng. 35 (1993) 359.
[5] U. Heiz, W.D. Schneider, J. Phys. D 33 (2000) 85.
[6] P. Wagner, A. Spudich, N. Ulman, C.E.D. Chidsey, J.A. Spudich, Biophys. J. 72 (1997) 452.
[7] V. Hlady, J. Buijs, Curr. Opin. Biotechnol. 7 (1996) 72.
[8] F.A. Denis, P. Hanarp, D.S. Sutherland, J. Gold, C. Mustin, P.G. Rouxhet, Y.F. Dufrene, Langmuir 18 (2002) 819.
[9] B. Kasemo, S. Johansson, H. Persson, P. Thormahlen, V.P. Zhdanov, Top. Catal. 13 (2000) 43.
[10] P.L.J. Gunter, J.W. Niemantsverdriet, F.H. Ribeiro, G.A. Somorjai, Catal. Rev. 39 (1997) 77.

[11] C. Werdinius, L. Österlund, B. Kasemo, Langmuir, in press.
[12] G.S. Zafiris, R.J. Gorte, J. Catal. 143 (1993) 86.
[13] J. Stubenrauch, J.M. Vohs, Catal. Lett. 47 (1997) 21.
[14] S. Johansson, L. Österlund, B. Kasemo, J. Catal. 201 (2001) 275.
[15] A. Holmgren, B. Andersson, D. Duprez, Appl. Catal. B 22 (1999) 215.
[16] C. Hardacre, R.M. Ormerod, R.M. Lambert, J. Phys. Chem. 98 (1994) 10901.
[17] D.W. Daniel, J. Phys. Chem. 92 (1998) 3891.
[18] S. Bernal, Catal. Today 50 (1999) 175.
[19] A. Törncrona, M. Skoglundh, P. Thormählen, E. Fridell, E. Jobson, Appl. Catal. B 14 (1997) 131.
[20] A. Trovarelli, Catal. Rev. Sci. Eng. 38 (1996) 439.
[21] V.P. Zhdanov, B. Kasemo, Appl. Surf. Sci. 135 (1998) 297.
[22] J. Sanz, J.P. Belzunegui, J. Rojo, J. Am. Chem. Soc. 114 (1992) 6749.
[23] S.J. Tauster, Acc. Chem. Res. 20 (1987) 389.
[24] S. Johansson, E. Fridell, B. Kasemo, J. Vac. Sci. Technol. A 18 (2000) 1514.
[25] V.K. Kaushik, Z. Phys. Chem. 173 (1991) 105.
[26] S. Bernal, J.J. Calvino, G. Cifredo, J.M. Rodriguez-Izquierdo, V. Perrichon, A. Laachir, J. Catal. 137 (1992) 1.
[27] J.G. Nunan, H.R. Robota, M.J. Cohn, S.A. Bradely, J. Catal. 133 (1992) 309.
[28] K.-E. Keck, B. Kasemo, Surf. Sci. 167 (1986) 313.
[29] M. Rinnemo, D. Kulginov, S. Johansson, K.L. Wong, V.P. Zhdanov, B. Kasemo, Surf. Sci. 376 (1997) 297.
[30] E.I. Altman, R.J. Gorte, Surf. Sci. 172 (1986) 71.
[31] S. Wohlrab, F. Winkelmann, J. Libuda, M. Bumer, H. Kuhlenbeck, H.J. Freund, in: R.J. Mc Donald, E.C. Taglauer, K. Wandelt (Eds.), Surface Science Principles, Springer, Berlin, 1996.
[32] M. Baumer, H.J. Freund, Prog. Surf. Sci. 61 (1999) 127.
[33] A. Holmgren, A. Fazlollah, E. Fridell, Appl. Catal. B 22 (1999).
[34] Y.F.Yu. Yao, J. Catal 87 (1984) 152.
[35] D.A. Frank-Kamenetskii, Diffusion and Heat Transfer in Chemical Kinetics, 2nd ed., Plenum, New York, 1969.
[36] K.L. Wong, S. Johansson, B. Kasemo, Faraday Discuss. 105 (1996) 237.
[37] K.H. Hansen, T. Worren, S. Stempel, L.E.M. Bäumer, H.-J. Freunde, F. Besenbacher, I. Stensgaard, Phys. Rev. Lett. 83 (1999) 4120.
[38] M.G.V. Mordente, C.H. Rochester, J. Chem. Soc. Faraday Trans. 85 (1989) 3495.